Study of KJ-66 micro gas turbine compressor: Steady and unsteady Reynolds-averaged Navier-Stokes approach

3 authors, including:

Junting Xiang
The Commonwealth Scientific and Industrial Research Organisation
27 PUBLICATIONS **187** CITATIONS

SEE PROFILE

Jorg Schluter
Deakin University
80 PUBLICATIONS **1,337** CITATIONS

SEE PROFILE

Study of KJ-66 micro gas turbine compressor: Steady and unsteady Reynolds-averaged Navier–Stokes approach

Junting Xiang[1], Jörg Uwe Schlüter[2] and Fei Duan[1]

Abstract

Numerical study on the compressor stage of a KJ-66 micro gas turbine was conducted in this paper through both steady and unsteady Reynolds-averaged Navier–Stokes. The study was conducted for the numerical prediction of micro gas turbine compressor performance at various operation conditions, with special attention given to the transient flow behaviors during compressor operation. The numerical results showed reasonable agreements with experimental data while providing predictions for the charting of compressor performance map at various operation speeds. The simulation results indicated that the increase of operation speed from 80 k r/min to 117 k r/min would leads to an increased peak total pressure ratio from 1.54 to 1.96, while decreasing the peak adiabatic efficiency from 0.73 to 0.55. This paper also provided discussion on details of transient flow field within the compressor stage as well as demonstrated the smooth flow transition through rotor–stator interactions.

Keywords

Micro gas turbine, compressor, Reynolds-averaged Navier–Stokes simulation, performance map

Date received: 3 January 2016; accepted: 23 March 2016

Introduction

Micro gas turbine (MGT) is a promising choice for unmanned aerial vehicles (UAV), due to the increasing demand for small size and endurance engine. Compared with other propulsion systems available for the UAV application, such as electric motor, solar panels, MGT is merited for its combination of higher thrust power, higher cruising speed, longer operation range, ability to operate with various fuels, etc.

Besides the extensive study regarding conventional gas turbines,[1–5] ongoing endeavors are made to understand the MGT performance.[6–11] MGT differs itself from conventional gas turbine due to its low operating Reynolds number and hence a relatively higher skin friction and heat transfer rate.[12,13] Existing research mainly focuses on the design of the engine,[14,15] combustor development,[16–18] combustion and emission,[9] combustion instability,[19,20] heat transfer,[21] control strategy,[22] etc. Specific study about the MGT compressor is still limited, although preliminary studies do have addressed this issue in some aspects. Mizuki et al.[23,24] have focused on developing the centrifugal compressor for ultra-MGT. By examining the compressor internal flow and performance characteristics, the design and manufacturing processes of the ultra-MGT centrifugal

compression system was explained. Zanger et al.[25] have experimentally investigated the pressure loss on the MGT compressor surge margin. Both steady-state and transient conditions were tested to aid the understanding of pressure loss. Fabian et al.[26] have introduced a capacitive measurement system for the MGT tip clearance. With a resolution of 0.8 μm, measurement range of 100 μm was achieved. Wang et al.[27] and Xi et al.[28] have endeavored to optimize the impeller and vane diffusor design collaboratively, for a 100 kW class MGT. Finite element stress analysis, surrogate model, and 3D viscous flow analysis have been carried out respectively, to achieve optimization of compressor components. Verstraete et al.[29] have numerically studied the heat transfer impact on the MGT compressor and turbine. A conjugate solver

[1]School of Mechanical and Aerospace Engineering, Nanyang Technological University, Singapore
[2]School of Engineering, Deakin University, Australia

Corresponding author:
Junting Xiang, School of Mechanical and Aerospace Engineering, Nanyang Technological University, 50 Nanyang Avenue, 639798, Singapore.
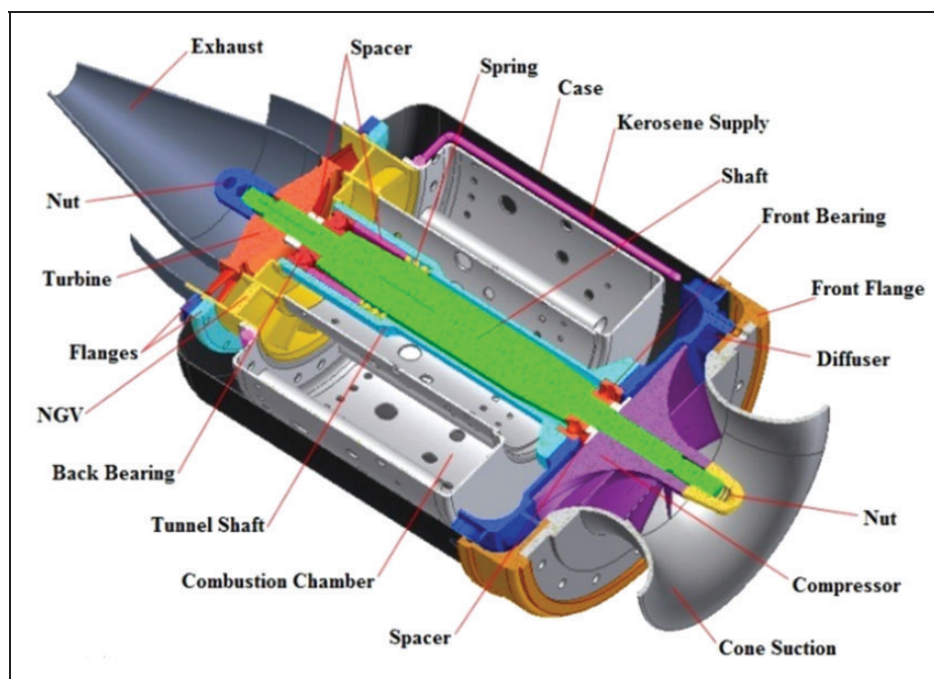Email: jtxiang@ntu.edu.sg

Figure 1. Layout of KJ-66 micro gas turbine.[38]

was developed, aiming to quantify and reveal contributing mechanisms of heat transfer. Steele et al.[30] have introduced the concept of combining shock compression system with conventional compressor design, to increase efficiency and reduce costs. The technology offered potential advantages of greater efficiency, fewer parts, lower weight, etc. Xiang et al.[31] have numerically investigated the effect of miniaturization, if a MGT compressor was built based on scaling of conventional gas turbine compressor. Ling et al.[32] and Olivero et al.[33] have carried out numerical analysis of the MGT centrifugal compressor respectively, and their work was merited in deepening the understanding of the micro compressor performance. Based on the previous work, more specific study about the MGT compressor, either with steady or unsteady simulations, is required.

In this study, numerical investigation of the KJ-66 MGT compressor is carried out, with steady and transient simulations, to deepen our understanding of the MGT compressor performance. Referring to our previous case study of NASA stage35 compressor,[34] the numerical setup of current study follow similar technique. Adjustment of specific operational conditions for the KJ-66 compressor is also addressed, according to its design parameters. The steady-state RANS simulations present reasonable consistence with the experimental data and predict the compressor performance map at changing operation speeds. The unsteady RANS simulation gives more details of transient flow behavior in the MGT compressor and shows smooth transition of flow through rotor–stator interactions.

Table 1. Design parameters and performance characteristics of KJ-66 MGT.[37]

Diameter	110 mm
Length	240 mm
Weight	0.93 kg
Number of compressor rotor blades	10
Number of compressor stator blades	15
Thrust	75 N
Maximum wheel speed	117,000 r/min
Compressor pressure ratio	2.2
Mass flow rate	0.22 kg/s
Maximum exhaust temperature	843 K

Design details of KJ-66 MGT compressor

In this study, the KJ-66 MGT is chosen because of its reliability and robustness and it is well tested. The combination of extreme conditions in terms of rotational speed with elevated gas temperatures makes MGT among the most advanced and complicated systems.

Figure 1 shows the layout of KJ-66 MGT and identification of each component. The single-stage centrifugal compressor is mounted at the engine entrance. The combustion chamber is located immediately after the compressor, followed by the turbine at the engine exit. More compact assembly is identified as smaller internal space is available, compared with conventional large gas turbine.[35]

Table 1 presents the design parameters and performance characteristics of KJ-66 MGT. The design
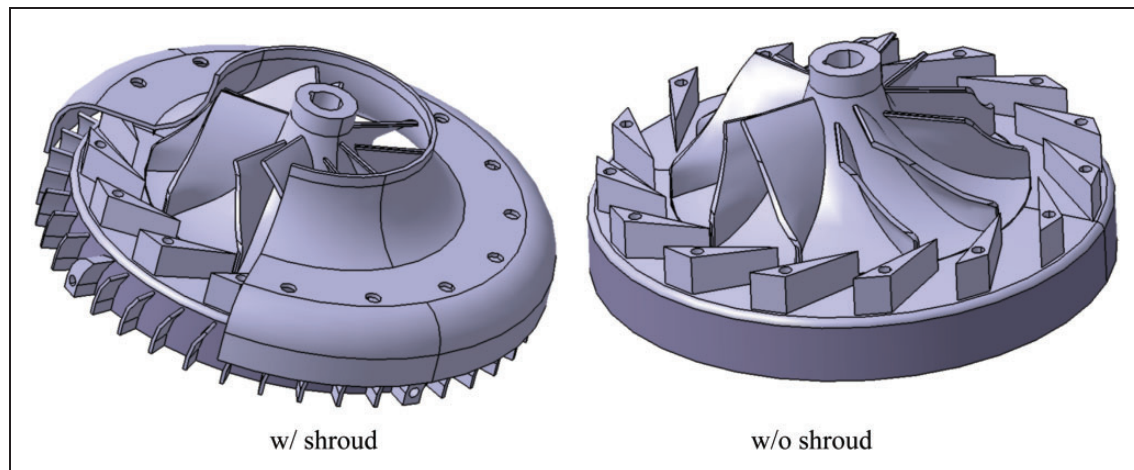
Figure 2. 3D model of KJ-66 MGT compressor: (a) w/ and (b) w/o shroud.

diameter and length demonstrates the small scale of MGT. In total, 10 rotor blades and 15 stator blades are built, with a design maximum rotational speed of 117,000 r/min, which is much faster than the conventional gas turbine engines.[36] With a design thrust of 75 N, the KJ-66 engine is widely recognized as an efficient model for the MGT study. The compressor pressure ratio is designed as 2.2 for the KJ-66 engine with only one compressor stage, which demonstrates the demand for high-performance compressor, as fewer compressor stages are available for MGT.

The centrifugal configuration of the KJ-66 compressor differs from the usual large engine compressor, where axial configuration of compressor is usually used. Our previous study of the NASA stage35 axial compressor has laid good reference for the current study.[34] All basic flow features from previous study are relevant for centrifugal compressor as well. Flow is accelerated and redirected towards the radial direction when it reaches the diffusor. Figure 2 shows the three-dimensional (3D) model of KJ-66 MGT centrifugal compressor, with (w/) and without (w/o) shroud, respectively. The twisting geometry of rotor blades is identified and the assembly of impeller and diffusor is also illustrated. The impeller has a tip radius of $R_{tip} = 33$ mm, with inlet hub and inlet shroud radius of $R_{ih} = 6.25$ mm and $R_{is} = 22.5$ mm, respectively. The inner diameter of the whole shroud is $D_{shroud} = 107.4$ mm. The splitter blades mounted after the compressor are also presented in the w/ shroud description, showing fluid is further redirected into axial direction before it enters the combustor.

Numerical approach setup

A similar approach for model generation with a NASA stage35 compressor[34] is utilized in this study. For the KJ-66 MGT compressor, due to concerns of computational time and resources, only one-fifth of the compressor is simulated with 72° azimuthally, consisting of two rotor blades and three stator
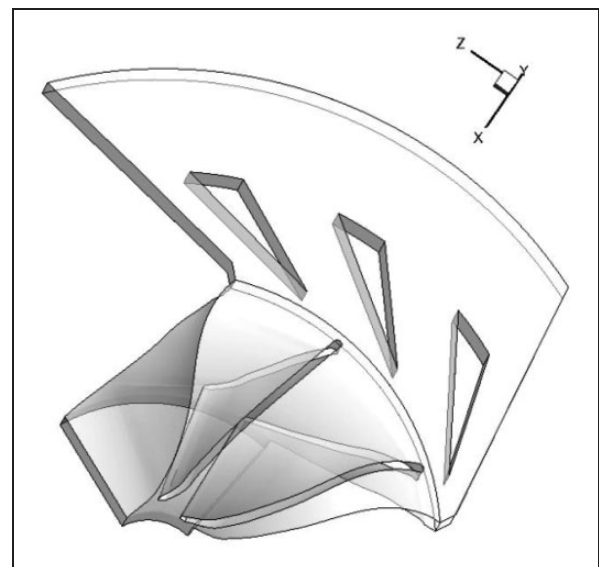

Figure 3. 3D view of the computational domain.

blades. Periodic boundary conditions are applied in the azimuthal direction to represent the full circular. Tip clearance is not considered currently to simplify our analysis. Although previous study indicates tip clearance flow leads to performance loss, especially for MGT,[39] the current study does not count in this effect to simplify our benchmark investigation. Further examination regarding this particular issue will be proposed and addressed in our follow-up study. Figure 3 shows the 3D view of the computational domain.

The computational domain is further subdivided into rotating impeller zone and stationary diffuser zone. Using Gambit_2.4, structured hexahedral meshes are generated for each zone separately, divided by interface surface. Each computational zone is further subdivided into sub-blocks, to aid mesh refinement based on block geometry. Mesh refinement is implemented near blade edge and near wall regions. Figure 4 shows the structured mesh built
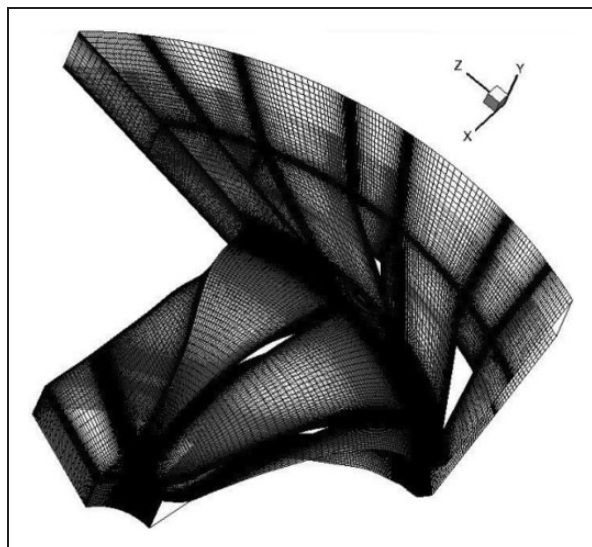
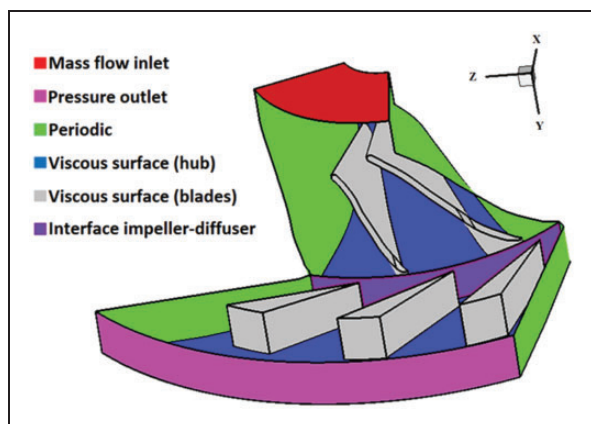**Figure 4.** Structured mesh for KJ-66 MGT compressor.

Figure 5. Specification of boundary conditions for KJ-66 MGT compressor.

for the KJ-66 MGT compressor. Local refinement of mesh generated can be identified. The grid independence study suggests that 1.3 million meshes are adequate for producing sufficiently accurate results.

Boundary conditions are specified referring to the previous case study,[40] with adjustment made according to the KJ-66 MGT compressor design parameters. Figure 5 shows the specification of boundary conditions and each boundary type is highlighted in different colors. Impeller entrance is defined as mass flow inlet boundary and diffuser exit is defined as pressure outlet boundary. The impeller–diffuser interface is highlighted in purple and periodic boundary is applied in the azimuthal direction and is highlighted in green. Wall boundary is defined as viscous surface, assuming fluid velocity is zero at wall.

Steady RANS simulation

The steady-state RANS simulation is carried out in ANSYS Fluent13.0, with parallel computing supported

by NTU HPC cluster. The Spalart–Allmaras turbulence model is used, due to its simplicity and its well-acceptance in turbomachinery community. Besides that, the mixing plane interface method is applied to tackle the rotor–stator interaction. These settings are identical with previous validation study.[40] The adiabatic wall condition is applied throughout this MGT study. The operation speed is defined as 80 k, 100 k, and 117 k r/min, with varying mass flow rate (M_{fr}) applied. Table 2 presents the details of boundary conditions and M_{fr} at various operation speeds. The applied M_{fr} is one-fifth of the real M_{fr} for the full compressor circular.

The first-order accuracy is initially enabled to accelerate the convergence and is switched to second order when a relatively low and stabilized residual is achieved. It takes approximately 10,000 iterations to reach the initial convergence, and a total of around 40,000 iterations to gain the confidence that final convergence is achieved.

Results from steady RANS simulations are then analyzed, to understand the operation of the MGT compressor and to determine the optimal operation point of the KJ-66 engine. Two essential values, the achieved total pressure ratio (Pr) and the efficiency loss, are taken as indication of compressor performance.

Figure 6 shows the distribution of total pressure ratio with varying M_{fr}, at different operation speeds. The simulation results are compared with the available experimental data from Murray's work,[41] where the compressor map is developed from the KJ-66 engine testing. From simulations, peak Pr value is observed for each operation speed, respectively. According to the design performance table, a $Pr = 2.2$ should be achieved with $M_{fr} = 0.22$ kg/s at 117 k r/min. However, simulation results produce peak $Pr = 1.96$ with $M_{fr} = 0.24$ kg/s at 117 k r/min. The Pr drops away from the optimal M_{fr} point. Result from simulations at 80 k r/min and 100 k r/min presents similar distribution, while smaller total pressure ratio is achieved with the decrease of operation speed. The peak $Pr = 1.54$ is achieved with $M_{fr} = 0.13$ kg/s at 80 k r/min, and peak $Pr = 1.76$ is achieved with $M_{fr} = 0.19$ kg/s at 100 k r/min, respectively. Generally, higher the operation speed, higher the Pr achieved. This is consistent with the experimental results, although deviations of the simulation and experimental results amplify with the increase of operation speed. This amplification of difference could be resulted from the insufficient capability of the simulation tool in capturing high-speed rotating flow, which requires further verifications. Generally, the simulation results underestimate the experimental data at higher operation speed.

Figure 7 shows the distribution of adiabatic efficiency with varying M_{fr}, at different operation speeds. Again, the simulation results are compared with the experimental data from Murray's work.[41]

Table 2. Details of boundary conditions and M_{fr} at various operation speeds.[41]

	Operation speed (r/min)		
	80 k r/min	100 k r/min	117 k r/min
Inlet temperature (k)	288		
Outlet temperature (k)	288		
Operating pressure (Pa)	0		
Inlet pressure (Pa)	101,325		
Outlet pressure (Pa)	131,325	161,325	202,325

Operation speed (r/min)					
80 k r/min		100 k r/min		117 k r/min	
Mass flow rate (kg/s)		Mass flow rate (kg/s)		Mass flow rate (kg/s)	
Input value	Real value	Input value	Real value	Input value	Real value
0.022	0.11	0.034	0.17	0.044	0.22
0.024	0.12	0.036	0.18	0.046	0.23
0.026	0.13	0.038	0.19	0.048	0.24
0.028	0.14	0.040	0.20	0.050	0.25
0.030	0.15	0.042	0.21	0.052	0.26
0.032	0.16	0.044	0.22	0.054	0.27
0.034	0.17	0.046	0.23	0.056	0.28
0.038	0.19	0.048	0.24	0.058	0.29
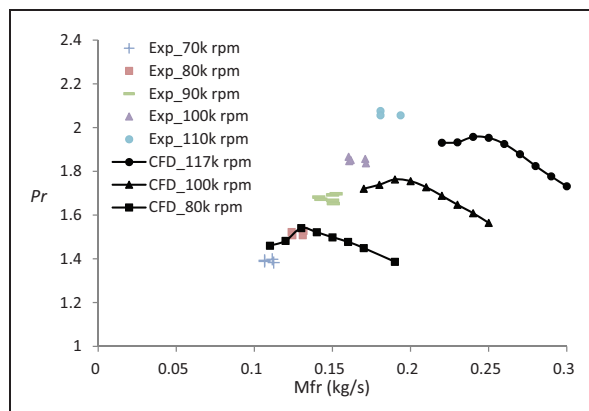
Figure 6. Distribution of simulation Pr with varying M_{fr} at different operation speeds.[41]
CFD: computational fluid dynamics.
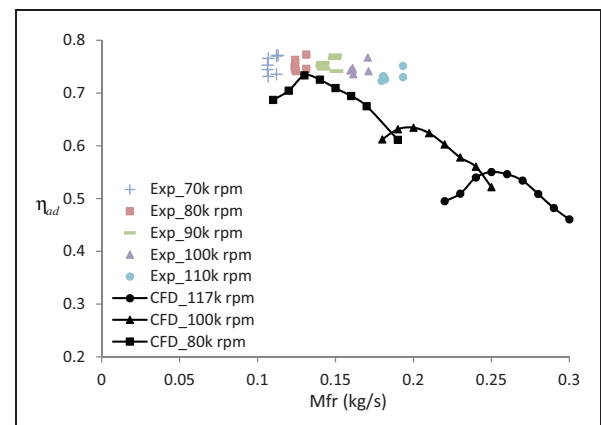
Figure 7. Distribution of simulation η_{ad} with varying M_{fr} at different operation speeds.[41]
CFD: computational fluid dynamics.

From simulations, peak η_{ad} value is observed for each operation speed, respectively. However, the value of η_{ad} generally decreases with the increase in operation speed, which is different from Pr distribution. At each operation speed, the η_{ad} drops away from the optimal M_{fr} point. The simulation results produce peak $\eta_{ad} = 0.73$ with $M_{fr} = 0.13$ kg/s at 80 k r/min, peak $\eta_{ad} = 0.63$ with $M_{fr} = 0.2$ kg/s at 100 k r/min, and peak $\eta_{ad} = 0.55$ with $M_{fr} = 0.25$ kg/s at 117 k r/min. Regarding each operation speed, the peak η_{ad} and peak Pr is identified with almost identical M_{fr}, indicating that value as the optimal operation M_{fr}. The experimental data present a declining trend of η_{ad} distribution, when operation speed increases from 70 k r/min to 110 k r/min. The simulation results

generally underestimate the experimental data, while similar declining trend of η_{ad} distribution is still captured. The simulations are conducted at ideal conditions and other affecting factors such as wall roughness, tip clearance flow, heat transfer from combustor, and so on are not taken into consideration. Slight difference in engine design used in experiments and simulations should also be mentioned.[37,41] These factors could lead to the deviations of compressor map generated from simulations and experiments.

The simulation results are further analyzed with regard to the flow structure within compressor. Figure 8 shows the distribution of total pressure within compressor and on rotor blade, with design
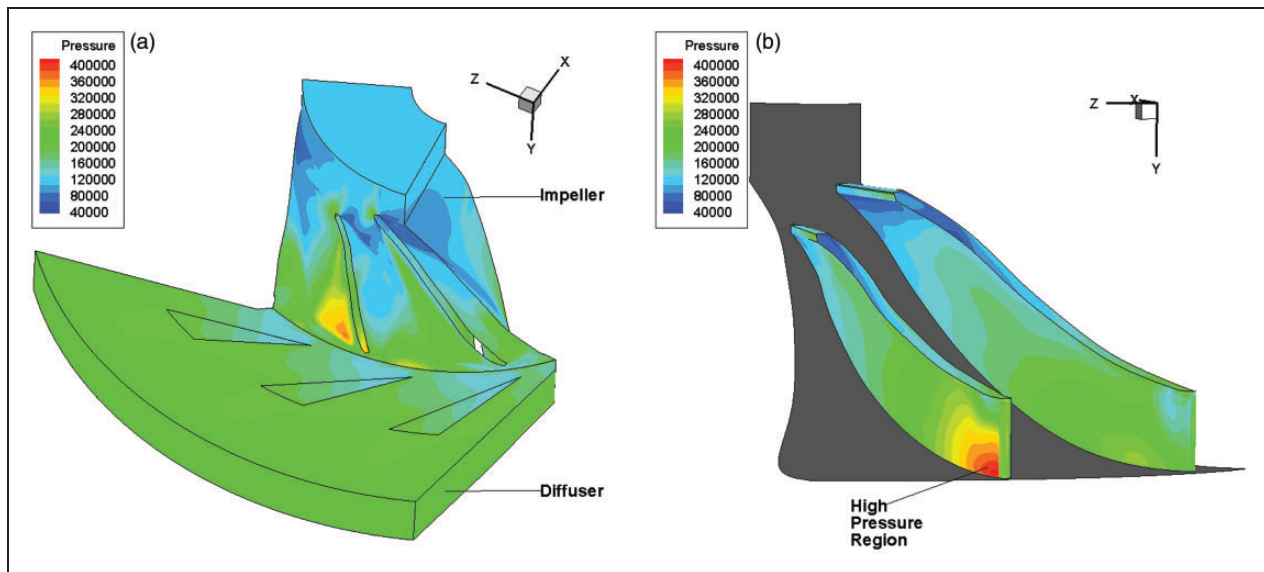
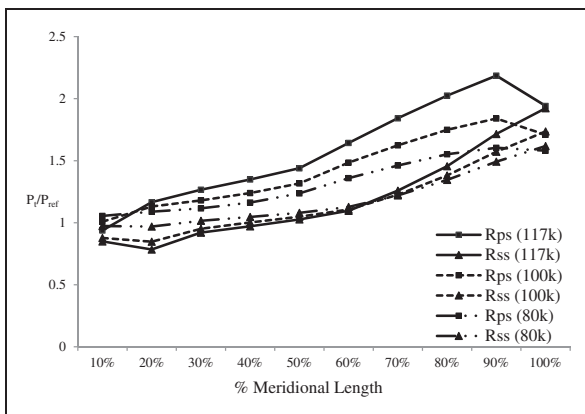**Figure 8.** Distribution of total pressure within compressor (a) and on rotor blade (b).

Figure 9. Distribution of total pressure on R_{ps} and R_{ss} along rotor meridional length, at different operation speeds.

M_{fr} at 117 k r/min. The gradual increase of total pressure along impeller streamwise is observed, with high total pressure region identified on the rotor pressure side (R_{ps}) near rotor trailing edge (R_{TE}).

Figure 9 further demonstrates the increase of total pressure along impeller streamwise, with design M_{fr} at 80 k, 100 k, and 117 k r/min, respectively. The total pressure at 10 meridional spans is presented, on both rotor suction side (R_{ss}) and R_{ps}. The total pressure value is normalized by the reference value at impeller inlets. At 117 k r/min, the observed *Pr* between rotor leading edge (R_{LE}) and R_{TE} is around 2, and it is the highest *Pr* achieved among the three operation speed cases. This indicates that *Pr* increases with the increase in operation speed. In addition, the theoretical blade work can also be obtained from the integral of total pressure difference between R_{ps} and R_{ss}. Therefore, the blade work also increases with the increase in operation speed, as the difference of total pressure between R_{ps} and R_{ss} increases.

The irreversibility within the KJ-66 MGT compressor is also considered. Figure 10 shows the distribution of radial velocity and entropy along impeller streamwise, with design M_{fr} at 117 k r/min. At the impeller entrance, the radial velocity is almost uniform, corresponding to nearly isentropic entropy distribution. However, small radial velocity is initially observed near R_{ss} close to the shroud when flow enters the in-between blade path. This indicates the occurrence of reversible flow due to false incidence angle, when incoming fluid attacks on R_{LE}. The generation of high entropy is also identified near R_{ss} close to shroud, indicating the incidence loss. As flow further propagates downstream, the small radial velocity region dissipates and expands towards R_{ps}, still mainly locating near the shroud. This indicates the secondary flow region and reversible flow, due to the streamwise and corner vortex. The high entropy region expands in similar pattern, suggesting the increase of η_{ad} loss along impeller streamwise.

The entropy distribution along impeller streamwise is further illustrated in Figure 11, where the entropy distribution on rotor blade with design M_{fr} at 117 k r/min and entropy distribution over impeller meridional length at three operation speeds are presented, respectively. The increase of entropy is observed along blade meridional length and high entropy is identified mainly near the impeller shroud, which is identical with discussion made earlier. The normalized entropy rise curve further illustrates the increase of entropy from R_{LE} to R_{TE}. In addition, the larger the operation speed, more entropy rise is identified, indicating more efficiency loss.

Figure 12 shows the streamline along impeller streamwise and diffuser streamwise, with design M_{fr} at 117 k r/min. The streamline in impeller is plotted in relative frame to counteract the effect of rotating
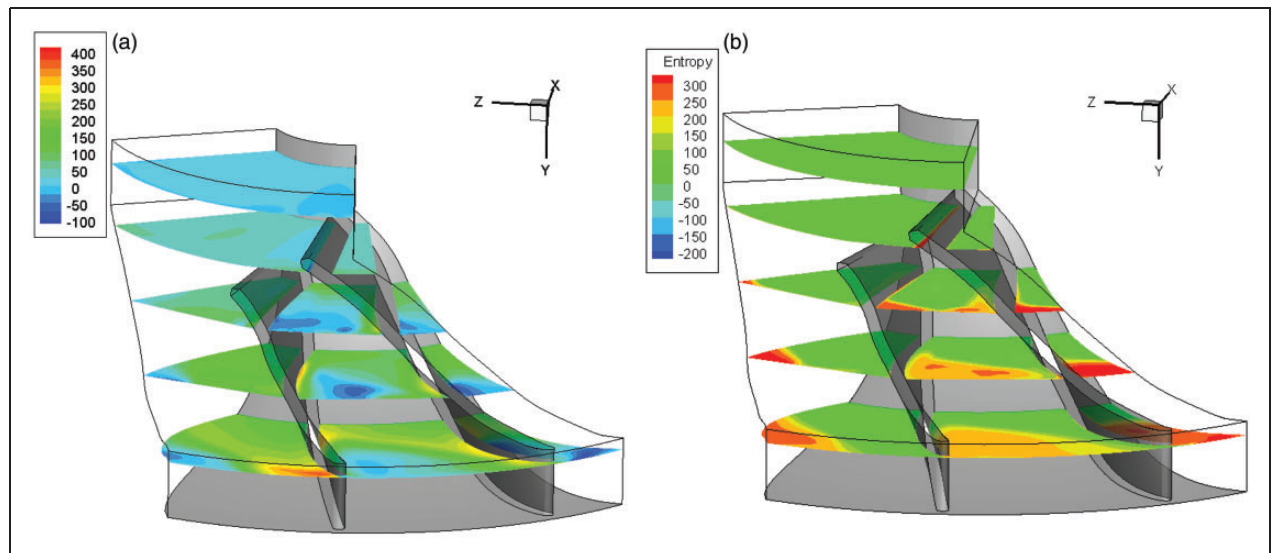
Figure 10. Distribution of radial velocity (a) and entropy (b) along impeller streamwise, with design M_{fr} at 117 k r/min.
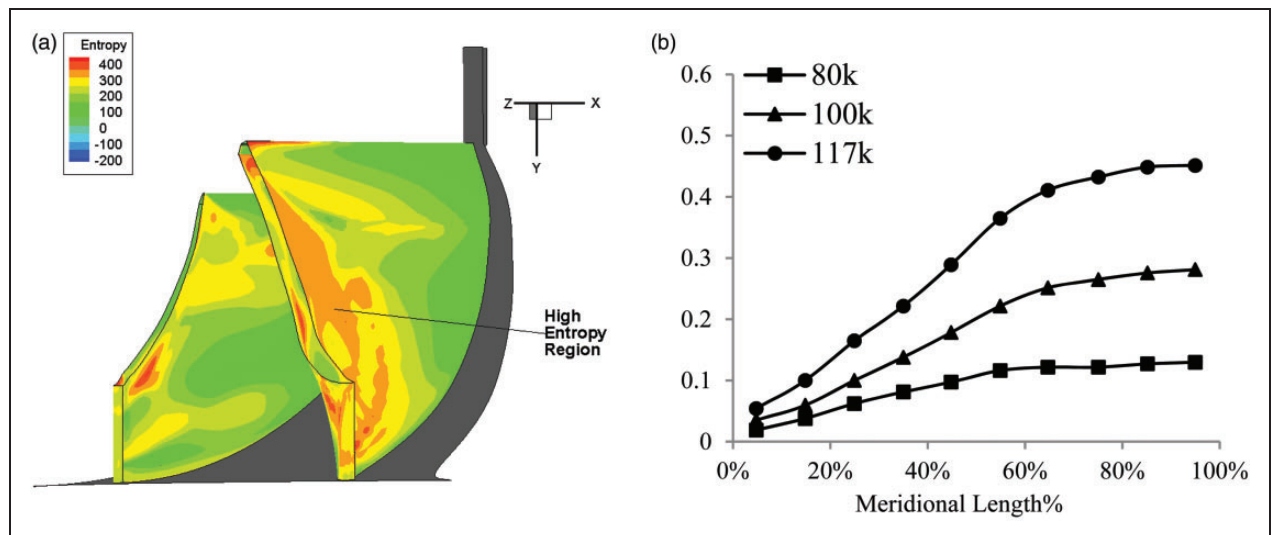

Figure 11. Distribution of entropy on rotor blade with design M_{fr} at 117 k r/min (a) and over impeller meridional length at different operation speeds (b).

rotor, while the streamline in diffuser is plotted in absolute frame. The reversible flow identified close to R_{ss} demonstrates the development of small radial velocity in the same region, due to streamwise and corner vortex. In the diffuser, vortex is also observed after the splitter blade, and the vortex moves from hub towards shroud. Further observation is presented in Figure 13, where the velocity vectors on 50% spanwise in the diffuser are shown. Strong vortex in the diffuser wake region can be identified and a zoom-in view shows the vortex behaves in clockwise pattern. In addition, as the vectors are colored by Mach value, a gradual decrease of flow Mach number is observed along the diffuser streamwise and small Mach region initiates near the stator trailing edge on stator pressure side.

Unsteady RANS simulation

Transient simulation of the KJ-66 compressor is then conducted, to provide more details of the flow development in compressor on time basis. Although grid independence is achieved with 1.3 million cells for steady-state simulations, we still increase the grid size to 2.54 million for this transient study, to more precisely identify flow structure changes along time.

Boundary conditions remain unchanged with the steady-state simulations except for the rotor–stator interface, where sliding mesh method is used instead of the previously utilized mixing plane method for steady-state simulations. The sliding mesh method is advantageous in more realistically capturing rotor–stator interactions, especially for
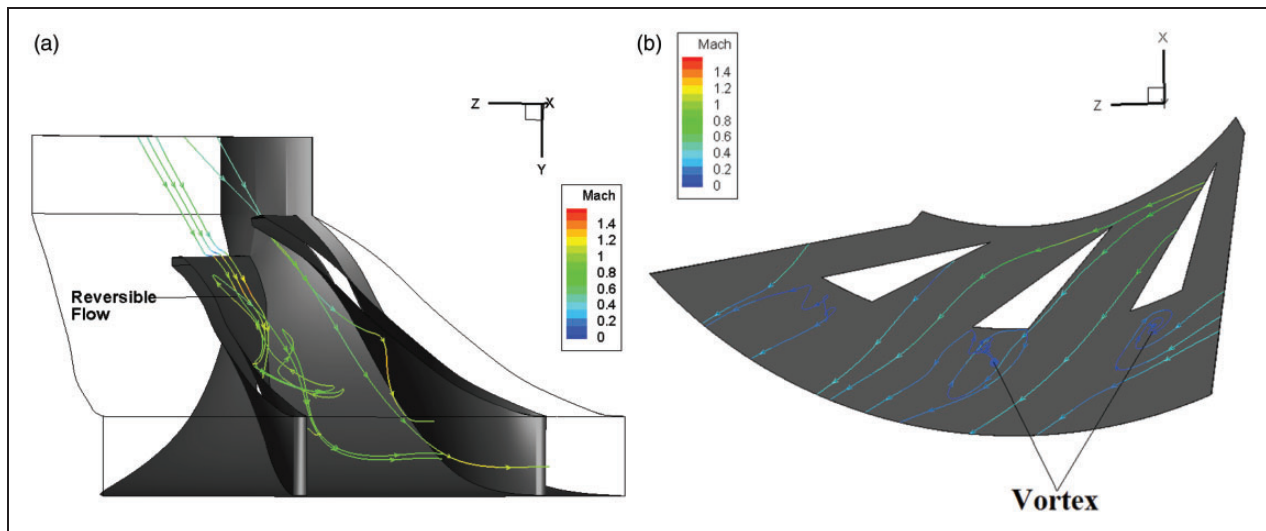
Figure 12. Streamline along impeller streamwise (a) and diffuser streamwise (b), with design M_{fr} at 117 k r/min.
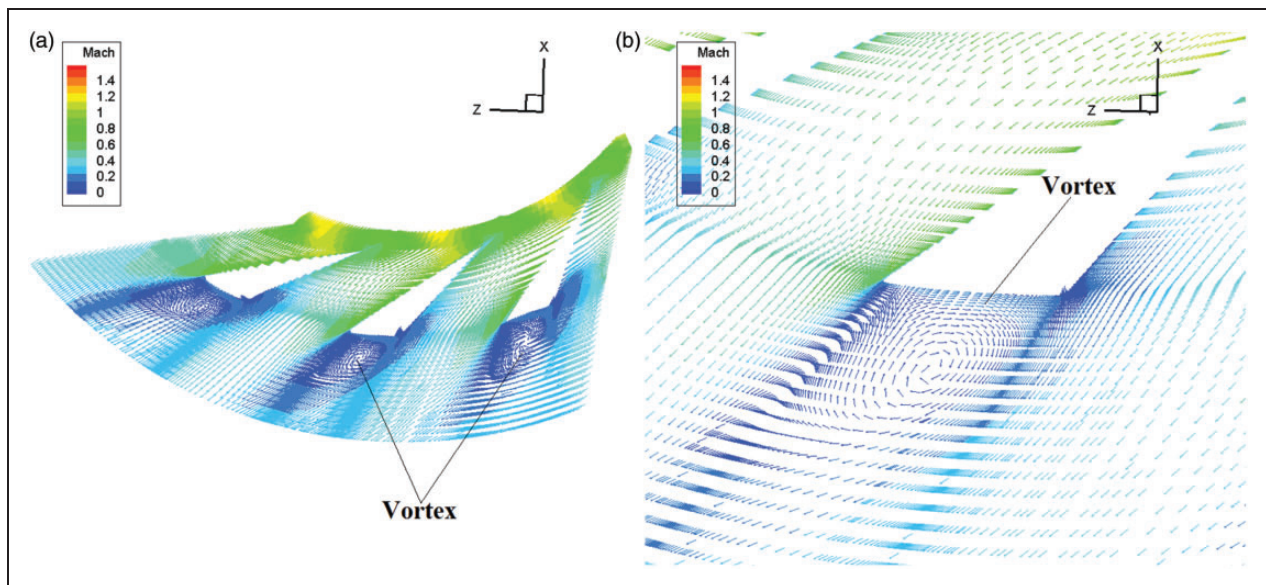

Figure 13. Velocity vectors on 50% spanwise in diffuser, normal view (a) and zoom-in view (b), with design M_{fr} at 117 k r/min.

compressor operating at high rotating speed. Besides that, a time step size $\Delta t = 3.9\,e$-06 s is defined based on experience and validation study, to ensure the accuracy of simulation and save computational efforts. Only the case with RPM $= 100$ k and $M_{fr} = 0.04$ kg/s is tested at the current stage and results are used for the analysis. Therefore, the compressor takes $t = 0.6\,e$–03 s to finish one revolution, requiring 154 time steps to accomplish. To ensure the flow is fully developed and for easy reference, a total running time of $t = 3.9\,e$–02 s is specified. It is equivalent to 10,000 time steps or 65 revolutions. Figure 14 shows the convergence history of M_{fr} monitored at diffuser outlet, from 90,000 to 100,000 iterations. It indicates periodic changes of M_{fr} during compressor operation while

also guaranteeing the mass balance as the average M_{fr} at diffuser outlet equaling to that at impeller inlet. The negative sign for M_{fr} here represents mass exiting the compressor system.

During operation, the impeller zone is moving with a high rotating speed while the diffusor zone remains stationary. Figure 15 shows the changes of impeller–diffusor assembly, colored by the static pressure contour. The first assembly in Figure 15(a) is taken from $t = 1.95\,e$–02 s, i.e. after 5000 time steps. The consequent time interval between each frame is $\Delta t' = 2.34\,e$–05 s, i.e. every 6 time steps. The impeller revolves along the rotor–stator interface from one end to another, and then returns to the initial end due to periodic boundary conditions to represent the full
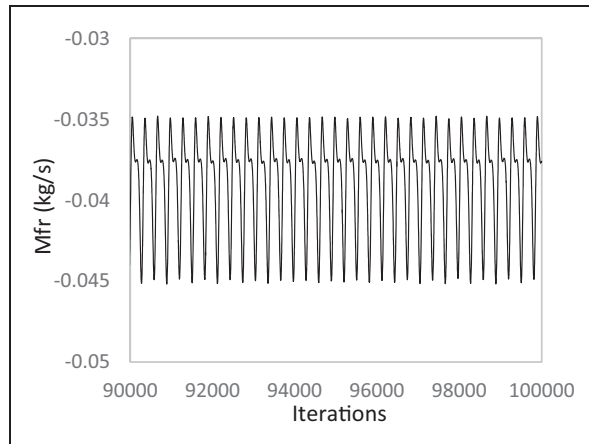
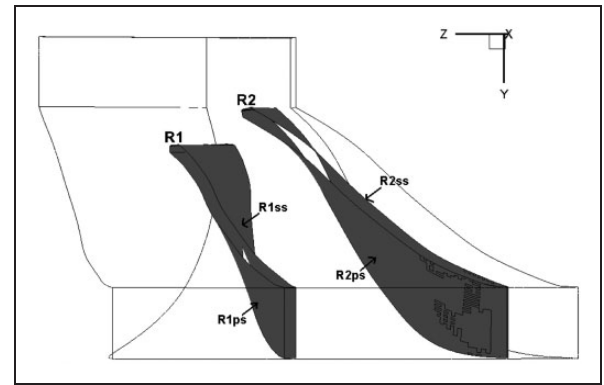Figure 14. Convergence history of M_{fr} at the diffuser outlet.
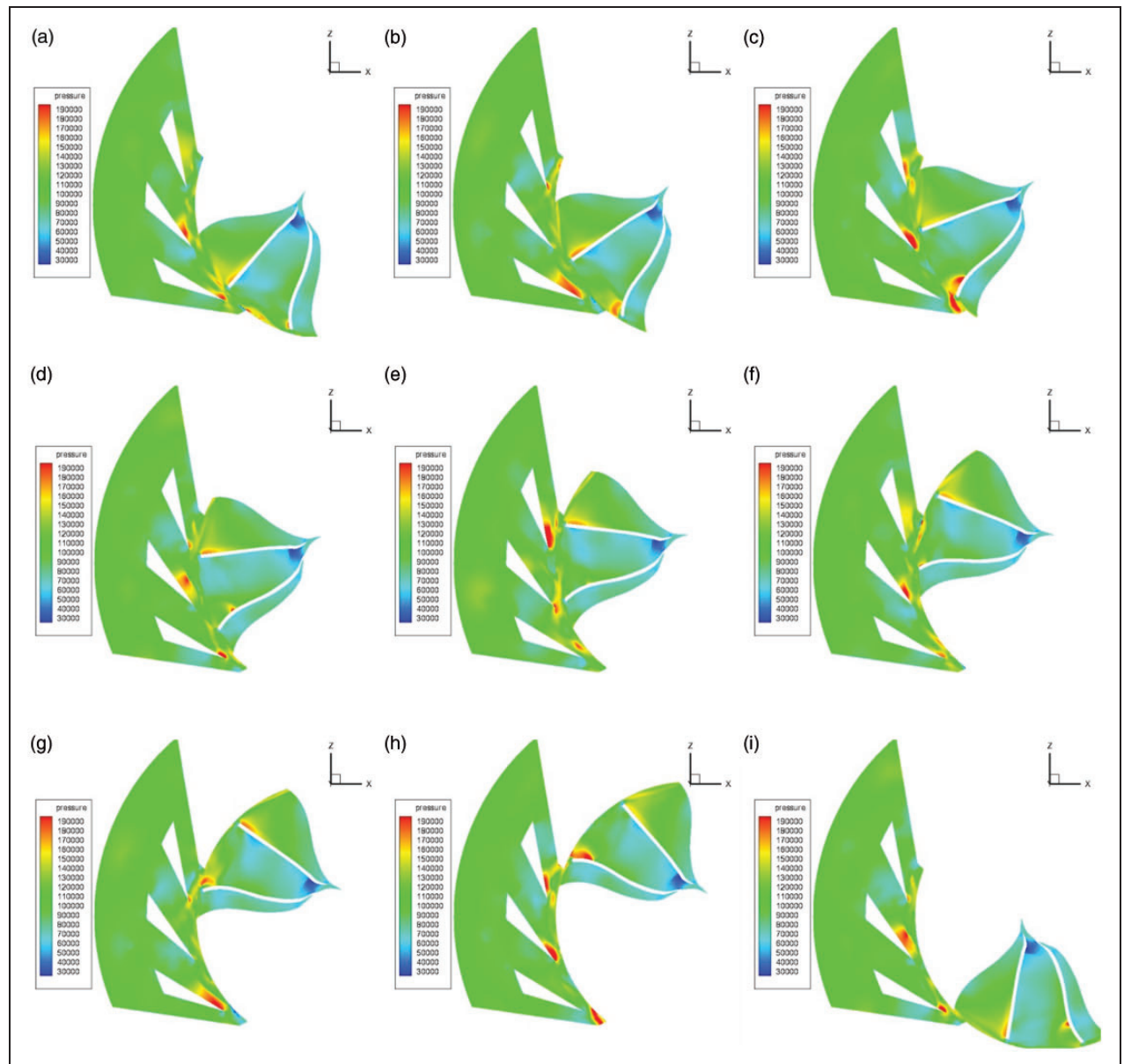

Figure 16. Definition of $R1$ and $R2$.

Figure 15. Changes of impeller–diffusor assembly along time: (a) $t = 1.95\,e{-}02$ s; (b) $t = 1.95234e{-}02$ s; (c) $t = 1.95468e{-}02$ s; (d) $t = 1.95702e{-}02$ s; (e) $t = 1.95936e{-}02$ s; (f) $t = 1.9617e{-}02$ s; (g) $t = 1.96404e{-}02$ s; (h) $t = 1.96638e{-}02$ s; (i) $t = 1.96872e{-}02$ s.
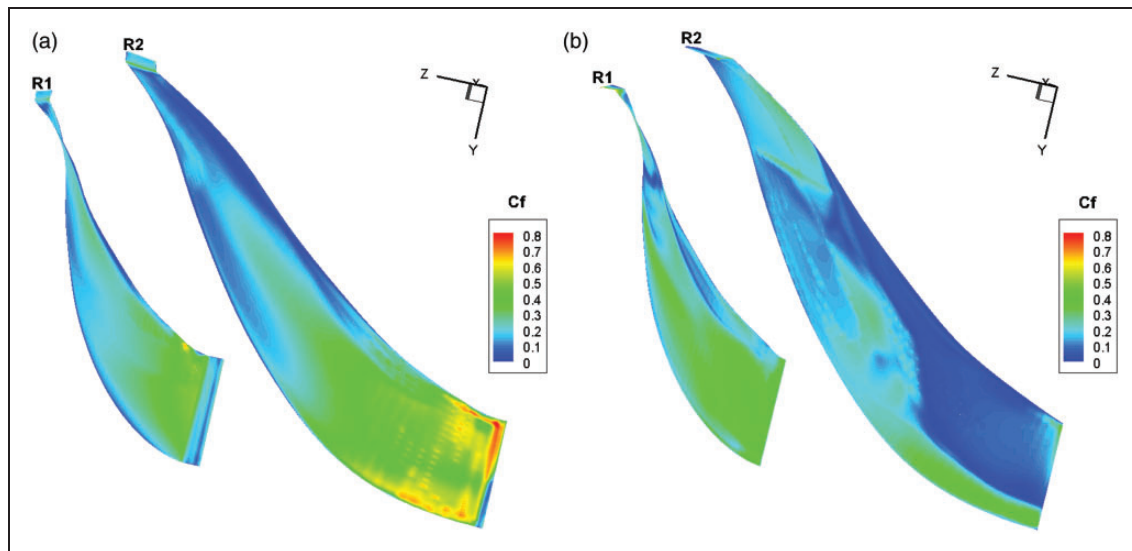
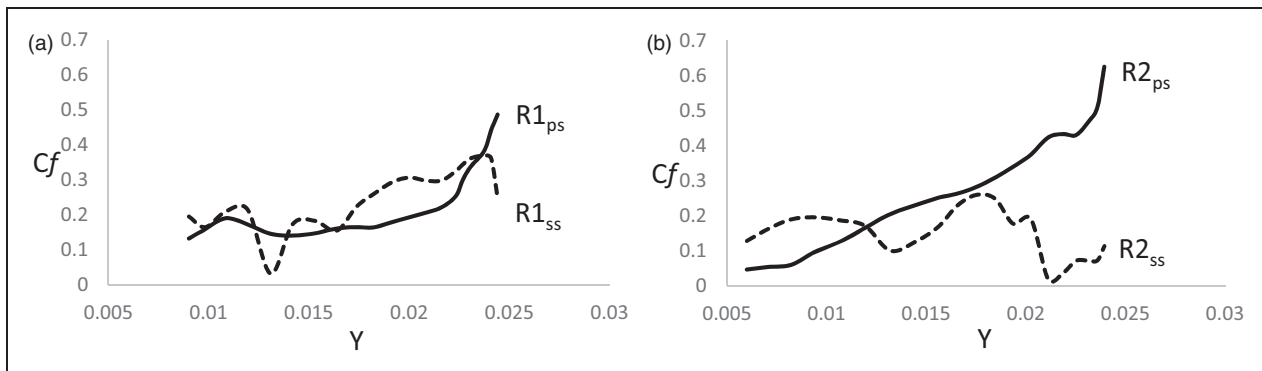**Figure 17.** Distribution of C*f* on R_{ps} (a) and R_{ss} (b).

Figure 18. Distribution of C*f* on R_{ps} and R_{ss}: (a) *R*1, splitter; (b) *R*2, main rotor.

circular. It clearly illustrates the change of impeller–diffusor alignment and the change of flow characteristics due to the change of blade coupling.

To more detailed understand the changes of flow property, simulation data from 100 k r/min test case at $t = 3.9\,\mathrm{e}{-}02\,\mathrm{s}$ are used for further analysis. Data from each of the two rotors, named *R*1 and *R*2, on their pressure and suction side surfaces, are drawn. Figure 16 points out the definition of *R*1 and *R*2. Actually, *R*2 is the main rotor and *R*1 is the splitter in impeller zone. It is named this way for simple reference.

To determine the boundary layer losses, the friction coefficient is usually referred. Equation (1) defines the friction coefficient C*f* as

$$\mathrm{C}f = \frac{\tau_w}{\frac{1}{2}\rho U_\infty^2} \tag{1}$$

where τ_w is the local wall shear stress and U_∞ is the free-stream velocity monitored at the inlet.

Figure 17 shows the C*f* contour on R_{ps} and R_{ss} on both of the rotors. Gradual increase of C*f* is identified
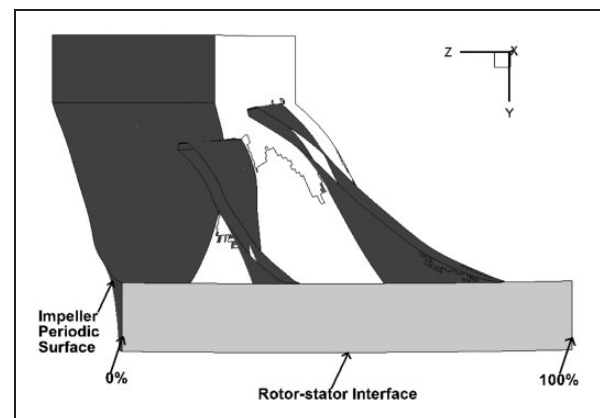

Figure 19. Rotor–stator interface and specification of data extraction points.

along the R_{ps}, for both *R*1 and *R*2. This can be caused by the boundary layer separation and the increased flow turbulence in the downstream. The C*f* also shows an increase trend on $R1_{ss}$, as it is more affected by the flow redirected from the main rotor *R*2. The C*f* shows
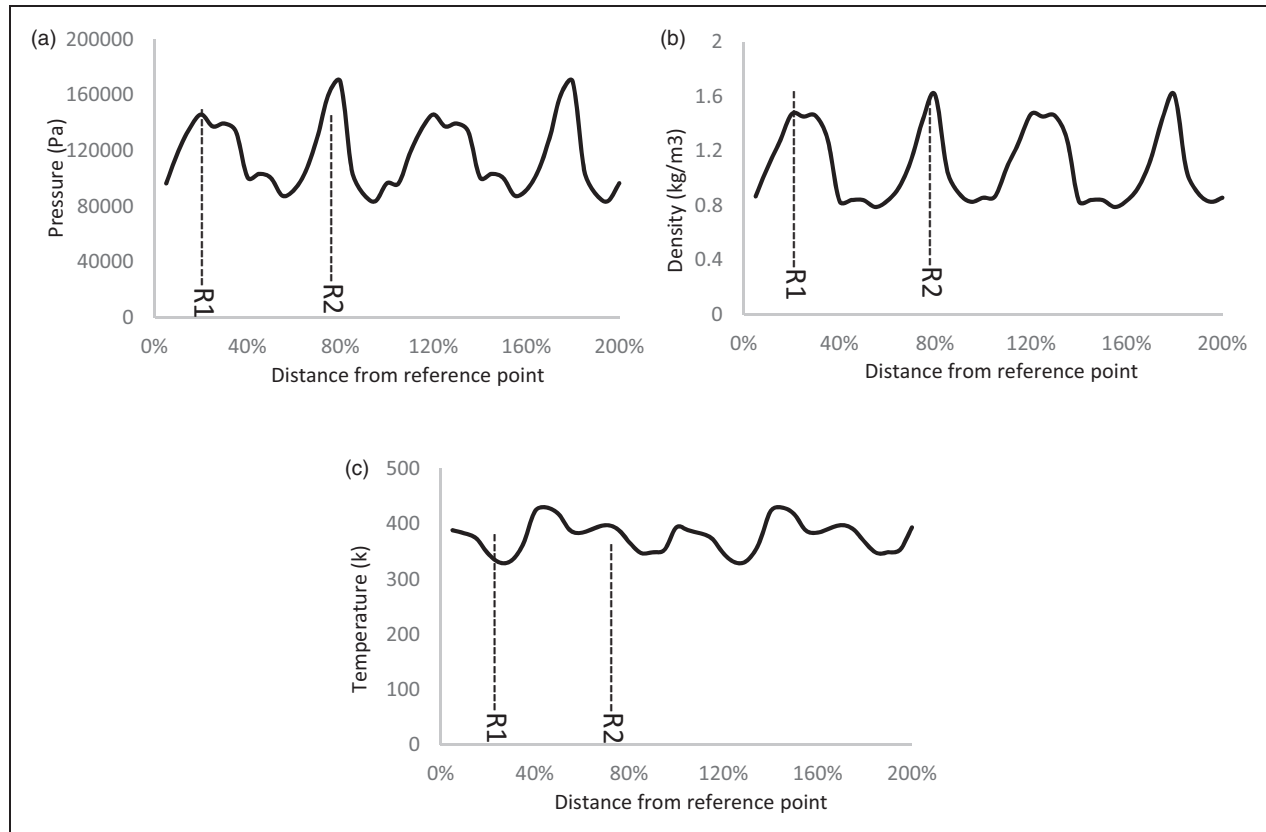
Figure 20. Flow properties change on rotor–stator interface.

no direct trend of increase on $R2_{ss}$, as it is slightly affected by flow from splitter $R1$. Figure 18 further shows the details of Cf from $R1$ and $R2$. Generally, R_{ps} results in more boundary layer losses, compared to R_{ss}. In addition, more losses are identified on the tail region of $R2_{ps}$.

The transition of flow properties at rotor–stator interface is of our concern. To aid our analysis, data from the interface surface are drawn, from locations 0% to 100% away from the impeller periodic surface, as shown in Figure 19.

The data points are further extended to 200%, representing impeller zone revolve anti-clockwise by 72° from top view, to show the periodicity of flow properties on interface. Figure 20 shows the details of flow properties change on rotor–stator interface. Figure 20(a) shows the variation of pressure on interface. An increase of pressure value is identified from mid-span region towards R_{ps}, after that, the pressure value decreases until reaches the mid-span region in the adjacent flow path. The peak value is observed near rotor blade and higher pressure value is identified near $R2$ blade. Periodic changes of pressure variation is expected on the interface region, and the variation follows a roughly sinusoid pattern. Figure 20(b) shows similar trend for density variation with that for pressure changes. A roughly sinusoid pattern of density is identified, where peak values are observed near rotor blades. This is not surprising,
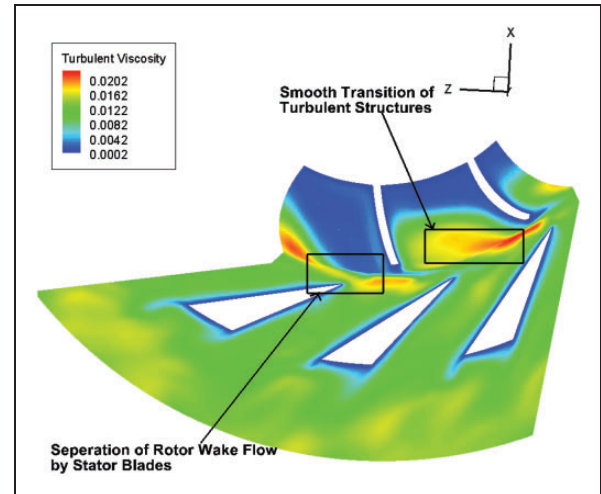
Figure 21. Transition of turbulent structure across rotor–stator interface.

as according to ideal gas law shown in the following equation

$$P = \rho R_{specific} T \tag{2}$$

where $R_{specific}$ is the specific gas constant. Gas pressure (P) is related to gas density (ρ) and gas temperature (T). Figure 20(c) shows the variation of gas temperature in the interface region. However, the extent of temperature variation is comparatively small, when
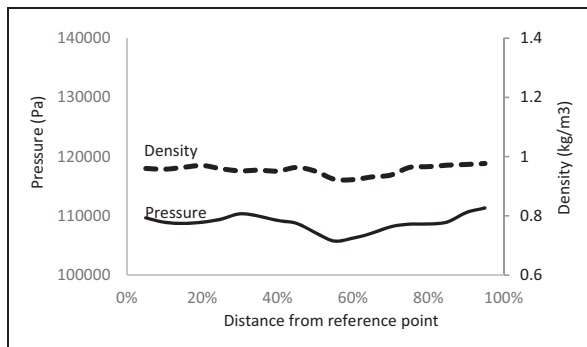
Figure 22. Distribution of pressure and density on diffusor outlet surface.

compared to the pressure variation. Therefore, gas density variation follows the trend of pressure distribution, as it is the dominant factor in this relation. This relation also answers why the pressurization of gas is necessary for gas turbines, as it leads to an increase in gas density and energy density before the combustion process occurs.

The transient simulation with sliding mesh technique enables the corresponding two interface zones to be interior. It accounts for the relative motions of rotating and stationary components. Therefore, fluxes across the interior are computed and transported smoothly. Figure 21 shows the transition of turbulent viscosity across the interface region, as an indication of the transition of turbulent structures. The flow becomes more turbulent in the downstream of impeller zone and further travels across the interface region. A smooth transition of turbulent structure can be identified, when flow enters the diffusor zone. The turbulent structure is further separated by the stator blades, before it enters the stator path. The peak turbulent viscosity diminishes and then sustains its value when it travels further downstream in the diffusor zone. Low turbulent viscosity region is identified near stator surface, due to the boundary layer effects.

Similar with the approach for analyzing the rotor–stator interface, data from the diffusor outlet surface are drawn, from locations 0% to 100% away from the diffusor periodic surface. Figure 22 shows the distribution of pressure and density on the diffusor outlet surface. Slight variations of both properties are observed on the diffusor outlet surface, indicating more even distribution of flow properties compared with that on the rotor–stator interface.

Results and discussion

In summary, the KJ-66 MGT compressor is numerically studied, with steady and unsteady RANS simulation. The steady RANS simulation investigated the KJ-66 compressor operation at three different speeds, i.e. 80 k, 100 k, and 117 k r/min, and it

presents reasonable consistence with the experiment data. With the increase in operation speed, the total pressure ratio shows an increasing pattern, while the adiabatic efficiency presents a declining trend. Simulation results underestimate the experimental value, for both total pressure ratio and adiabatic efficiency. The unsteady RANS simulation gives more details of transient flow behavior during compressor operation and it deepens our understanding of the MGT compressor performance characteristics. Flow field is analyzed to address the rotor–stator interaction and technique applied ensures smooth transition of flow between the rotating and stationary zones.

In this study, we have adopted the numerical approach validated in our previous endeavors. Although reasonable predictions are achieved for this MGT compressor performance, some limitations still require clarifications. For MGT radial compressor, the tip loss is expected to be more significant, the surface area for heat transfer is much greater, and the friction on the shroud is a major source of loss. It requires further investigations to address these issues. Nevertheless, the current study is still merited in broadening the knowledge of the MGT compressor.

Declaration of conflicting interests

The author(s) declared no potential conflicts of interest with respect to the research, authorship, and/or publication of this article.

References

1. Schluter JU, Wu X, Kim S, et al. A framework for coupling reynolds-averaged with large-eddy simulations for gas turbine applications. *J Fluids Eng* 2005; 127: 806–815.
2. Schluter JU, Wu X, Kim S, et al. Coupled RANS-LES computation of a compressor and combustor in a gas turbine engine. In: *40th AIAA/ASME/SAE/ASEE joint propulsion conference and exhibit, joint propulsion conferences*, Fort Lauderdale, FL, USA, 2004.
3. Schluter JU, Wu X, van der Weide, et al. Integrated LES-RANS of an entire high- spool of a gas turbine. In: *4th AIAA aerospace sciences meeting and exhibit*, Reno, Nevada, USA, 2006.
4. Gourdain N. Prediction of the unsteady turbulent flow in an axial compressor stage. Part 1: Comparison of unsteady RANS and LES with experiments. *Comput Fluids* 2015; 106: 119–129.

5. Gourdain N. Prediction of the unsteady turbulent flow in an axial compressor stage. Part 2: Analysis of unsteady RANS and LES data. *Comput Fluids* 2015; 106: 67–78.

6. Dessornes O, Landais S, Valle R, et al. Advances in the development of a microturbine engine. *J Eng Gas Turbines Power* 2014; 136: 071201.

7. Zhang X-Q, Wang X-L, Liu R, et al. Modeling and analysis of micro hybrid gas spiral-grooved thrust bearing for microengine. *J Eng Gas Turbines Power* 2013; 135: 122508.

8. Christodoulou F, Giannakakis P and Kalfas AI. Performance benefits of a portable hybrid micro-gas turbine power system for automotive applications. *J Eng Gas Turbines Power* 2010; 133: 022301.

9. Liu C-R and Shih H-Y. Model analysis of syngas combustion and emissions for a micro gas turbine. *J Eng Gas Turbines Power* 2015; 137: 061507.

10. Cadorin M, Pinelli M, Vaccari A, et al. Analysis of a micro gas turbine fed by natural gas and synthesis gas: MGT test bench and combustor CFD analysis. *J Eng Gas Turbines Power* 2012; 134: 071401.

11. Hany M. Future technology challenges for small gas turbines. In: *AIAA international air and space symposium and exposition: The next 100 years*, AIAA 2003-2559, Dayton, Ohio, USA, 2003.

12. Gong Y, Sirakov BT, Epstein AH, et al. Aerothermodynamics of micro-turbomachinery. *Proceedings of the ASME turbo expo*, Vienna, Austria, 2004, pp.95–102.

13. Sirakov B, Gong Y, Epstein A, et al. Design and characterization of micro-compressor impellers. *2004 ASME turbo expo*, Vienna, Austria, 14–17 June 2004, pp.737–746.

14. Aichmayer L, Spelling J, Laumert B, et al. Micro gas-turbine design for small-scale hybrid solar power plants. *J Eng Gas Turbines Power* 2013; 135: 113001.

15. Vézina G, Fortier-Topping H, Bolduc-Teasdale F, et al. Design and experimental validation of a supersonic concentric micro gas turbine. *J Turbomach* 2015; 138: 021007.

16. Takashi S and Saburo Y. Development of a hydrogen-fueled pulse detonation combustor for 1 kW-class micro gas turbine. In: *46th AIAA/ASME/SAE/ASEE joint propulsion conference & exhibit*, AIAA 2010-6881, Nashville, TN, USA, 2010.

17. Saburo Y and Kana O. Concept and experiment of a flat-flame microcombustor for ultra micro gas turbine. In: *38th AIAA/ASME/SAE/ASEE joint propulsion conference & exhibit,* AIAA 2002-3771, Indianapolis, Indiana, USA, 2002.

18. Katsuhiro M, Takeshi M, Saburo Y, et al. Development of a hydrogen-fueled micro gas turbine with a lean premixed combustor. In: *33rd joint propulsion conference and exhibit*, AIAA 1997-3388, Seattle, WA, USA, 1997.

19. Li L and Zhao D. Prediction of stability behaviors of longitudinal and circumferential eigenmodes in a choked thermoacoustic combustor. *Aerosp Sci Technol* 2015; 46: 12–21.

20. Li X and Zhao D. Feedback control of self-sustained nonlinear combustion oscillations. *J Eng Gas Turbines Power* 2015; 138: 061505.

21. Verstraete T, Alsalihi Z and van den Braembussche RA. Numerical study of the heat transfer in micro gas turbines. *J Turbomach* 2006; 129: 835–841.

22. Ferrari ML, Pascenti M, Magistri L, et al. A micro gas turbine based test rig for educational purposes. *J Eng Gas Turbines Power* 2010; 132: 024502 (5 pp).

23. Mizuki S. Development of compressor for ultra micro gas turbine. *J Therm Sci* 2007; 16: 19–27.

24. Mizuki S, Hirano T, Koizumi Y, et al. Design and prototyping of micro centrifugal compressor for ultra micro gas turbine. *J Therm Sci* 2005; 14: 308–313.

25. Zanger J, Widenhorn A and Aigner M. Experimental investigations of pressure losses on the performance of a micro gas turbine system. *J Eng Gas Turbines Power* 2011; 133.

26. Fabian T, Sangkyun K and Prinz F. Capacitive blade tip clearance measurements for a micro gas turbine. *Proceedings of the 19th IEEE instrumentation and measurement technology conference*, Piscataway, NJ, USA. vol. 2: 2002, pp.1011–1015.

27. Wang H-L and Xi G. Optimization of high speed centrifugal compressor for a micro gas turbine based on CFD and FEM analysis. In: *Proceedings of the ASME turbo expo*, Glasgow, UK, GT 2010-22863, 2010, pp.439–446.

28. Xi G, Wang Z, Zhang C, et al. Aerodynamic optimization design of vaned diffusers for the 100KW micro gas turbine's centrifugal compressor. In: *Proceedings of the ASME turbo expo*, Berlin, Germany, GT2008-50440, 2008, pp.2297–2303.

29. Verstraete T, Alsalihi Z and van den Braembussche RA. Numerical study of the heat transfer in micro gas turbines. *J Turbomach Trans ASME* 2007; 129: 835–841.

30. Steele R, Baldwin P and Kesseli J. Insertion of shock wave compression technology into micro turbines for increased efficiency and reduced costs. In: *Proceedings of the ASME turbo expo*, Reno-Tahoe, NV, USA, 2005, pp.857–862.

31. Xiang J, Schlüter JU and Duan F. Miniature gas turbines: Numerical study of the effects of heat transfer and Reynolds number on the performance of an axial compressor. *Int J Comput Mater Sci Eng* 2014; 3: 1450008.

32. Ling J, Wong KC and Armfield S. Numerical investigation of a small gas turbine compressor. *Proceedings of the 16th Australasian fluid mechanics conference*. Australia: University of Queensland, 2007, pp.961–966.

33. Olivero M, Javed A and van Buijtenen JP. Aerodynamic analysis of a micro turbine centrifugal compressor. In: *Proceedings of the ASME turbo expo*, Glasgow, Scotland, GT 2010-23112, 2010, pp.2043–2052.

34. Xiang J, Schluter JU and Duan F. Towards simulation of NASA35 axial compressor. *Aircraft Eng Aerosp Technol J* 2015; 87.

35. Reid L and Moore RD. Performance of single-stage axial-flow transonic compressor with rotor and stator aspect ratio of 1.19 and 1.26, respectively, and with design pressure ratio of 1.82. NASA Technical Paper, 1978, p. 1338.

36. Reid L and Moore RD. Design and performance of four highly loaded, high speed inlet stages for an advanced high pressure ratio core compressor. NASA Technical Paper, 1978, p. 1337.
37. KJ66 engine designs. http://wwwgtbacouk/engine_designs/kj66htmGas Turbine Builders Association.
38. L.T. KJ-66 micro gas turbine layout. http://appliedcfd-com/cfd_microturbineshtm2004.
39. Xiang J, Schluter JU and Duan F. Effects of tip clearance on miniature gas turbines compressor performance: A numerical approach. In: *33rd AIAA applied aerodynamics conference*, Dallas, TX, USA, AIAA 2015-2412, 2015.
40. Xiang J, Schlüter JU and Duan F. CFD validation and analysis of a single-stage axial compressor. *Appl Mech Mater* 2014; 629: 109–118.
41. Murray PW. *Microturbine for micro-cogeneration application*. Master Thesis, Queen's University, Canada, 2009. http://qspacelibraryqueensuca/bitstream/1974/5237/1/Murray_Paul_W_200909_MScEngpdf.

Appendix

Notation

Cf	friction coefficient
M_{fr}	mass flow rate (kg/s)
Pr	total pressure ratio
R_{ps}	rotor pressure side
R_{ss}	rotor suction side
R_{TE}	rotor trailing edge
R_{LE}	rotor leading edge
η_{ad}	adiabatic efficiency